LAWRENCE
LIVERMORE
NATIONAL
LABORATORY

LLNL-JRNL-409682

Optimizing stability, transport, and divertor operation through plasma shaping for steady-state scenario development in DIII-D

C. T. Holcomb, J. R. Ferron, T. C. Luce, T. W. Petrie, P. A. Politzer, T. L. Rhodes, E. J. Doyle, M. A. Makowski, C. Kessel, J. C. DeBoo, R. J. Groebner, T. H. Osborne, P. B. Snyder, C. M. Greenfield, R. J. La Haye, M. Murakami, A. W. Hyatt, C. Challis, R. Prater, G. L. Jackson, J.-M. Park, H. Reimerdes, A. D. Turnbull, G. R. McKee, M. W. Shafer, M. Groth, G. D. Porter, W. P. West

January 7, 2009

Physics of Plasmas

Disclaimer

This document was prepared as an account of work sponsored by an agency of the United States government. Neither the United States government nor Lawrence Livermore National Security, LLC, nor any of their employees makes any warranty, expressed or implied, or assumes any legal liability or responsibility for the accuracy, completeness, or usefulness of any information, apparatus, product, or process disclosed, or represents that its use would not infringe privately owned rights. Reference herein to any specific commercial product, process, or service by trade name, trademark, manufacturer, or otherwise does not necessarily constitute or imply its endorsement, recommendation, or favoring by the United States government or Lawrence Livermore National Security, LLC. The views and opinions of authors expressed herein do not necessarily state or reflect those of the United States government or Lawrence Livermore National Security, LLC, and shall not be used for advertising or product endorsement purposes.

Optimizing stability, transport, and divertor operation through plasma shaping for steady-state scenario development in DIII-D

C.T. Holcomb[1], J.R. Ferron[2], T.C. Luce[2], T.W. Petrie[2], P.A. Politzer[2], T.L. Rhodes[3], E.J. Doyle[3], M.A. Makowski[1], C. Kessel[4], J.C. DeBoo[2], R.J. Groebner[2], T.H. Osborne[2], P.B. Snyder[2], C. M. Greenfield[2], R.J. La Haye[2], M. Murakami[5], A.W. Hyatt[2], C. Challis[6], R. Prater[2], G.L. Jackson[2], J.-M. Park[5], H. Reimerdes[7], A.D. Turnbull[2], G.R. McKee[8], M.W. Shafer[8], M. Groth[1], G.D. Porter[1], and W.P. West[2]

[1]Lawrence Livermore National Laboratory, Livermore, California, USA

[2]General Atomics, San Diego, California, USA

[3]University of California, Los Angeles, California, USA

[4]Princeton Plasma Physics Laboratory, Princeton, New Jersey, USA

[5]Oak Ridge National Laboratory, Oak Ridge, Tennessee, USA

[6]Association Euratom-UKAEA, Abingdon, UK

[7]Columbia University, New York, New York, USA

[8]University of Wisconsin, Madison, Wisconsin, USA

Abstract. Recent studies on DIII-D have elucidated key aspects of the dependence of stability, confinement, and density control on the plasma magnetic configuration, leading to the demonstration of nearly non-inductive (i.e., total inductive current ≈ 0) operation for >1 s with pressure 30% above the ideal no-wall stability limit. Achieving fully noninductive operation requires high pressure, good confinement, and density control through divertor pumping. Plasma geometry affects all of these. Ideal MHD modeling of external kink stability suggests it may be optimized by adjusting the shape parameter known as squareness (ζ). Optimizing kink stability means increasing the maximum stable pressure. Experiments confirm stability varies strongly with ζ, in agreement with the modeling. Optimization of kink stability via ζ is concurrent with an increase in the H-mode edge pressure pedestal stability. Global energy confinement is optimized at the lowest ζ tested, consistent with increased pedestal pressure and lower core transport. Adjusting the magnetic divertor balance about a double-null (DN) configuration optimizes density control for improved noninductive auxiliary current drive. The best density control is obtained with a slight imbalance toward the divertor opposite the ion grad(B) drift direction, consistent with modeling of these effects. These optimizations have been combined to achieve non-inductive current fractions near 1 for over 1 s with normalized pressure ~3.5–3.7, bootstrap current fraction >65%, and a normalized confinement factor $H_{98(y,2)} \approx 1.5$.

PAC Nos:

I. INTRODUCTION

Advanced tokamak research on DIII-D[1] is focused on developing a high fusion gain, steady-state scenario that would eliminate or greatly reduce the demands on an inductive transformer in future machines. Steady-state operation requires the inductively driven current density (j_{Ind}) be zero everywhere.[2] Most of the total current I_{p} must be from self-driven bootstrap current,[3] with the remainder driven by external noninductive sources, such as neutral beam and radiofrequency current drive. Previously reported DIII-D results[4,5] achieved bootstrap fractions $f_{\mathrm{BS}} \equiv I_{\mathrm{BS}}/I_{\mathrm{p}}$ between 50% and 70%, neutral beam current drive fraction f_{NB} up to 40%, and the remainder driven by electron cyclotron current drive (ECCD) and/or inductive current. It is relatively straightforward to achieve noninductive current fraction $f_{\mathrm{NI}} = I_{\mathrm{NI}}/I_{\mathrm{p}} \sim 90\%$ for about a current relaxation time,[6] but $f_{\mathrm{NI}} =$ 100% has so far been difficult to achieve except transiently. The current relaxation time $\tau_{\mathrm{R}} \equiv 0.17R/\Re$ is the time constant of the lowest order spatial eigenmode of the current evolution equation with the constraint of constant current, where R is the major radius in meters and $\Re$ is the plasma resistance in $\mu\Omega$.[7]

This paper describes an extension of the $f_{\mathrm{NI}} \sim 100\%$ condition to $\sim 0.7\tau_{\mathrm{R}}$ that was achieved by a combination of technical improvements and new scientific insights. The insights are an optimization of the plasma shape parameter known as squareness and an optimization of divertor magnetic balance to simultaneously improve stability, confinement, and density control. These are each essential for achieving fully noninductive operation. Bootstrap current fraction f_{BS} is proportional to normalized beta, $\beta_{\mathrm{N}} = \beta_{\mathrm{T}}(\%)\big/\left[I_{\mathrm{p}}(\mathrm{MA})/a(\mathrm{m})B_{\mathrm{T}}(\mathrm{T})\right]$, where $\beta_{\mathrm{T}} = 2\mu_0\langle p\rangle\big/B_{\mathrm{T}}^2$ is the toroidal beta, a

is the equivalent minor radius and B_T the toroidal field). It is desirable to operate at the highest stable β_N, assuming the resulting j_{BS} is well aligned with j_{total}.[8] Experiments to achieve steady-state operation on DIII-D typically run above the ideal $n = 1$ kink mode limit without a conducting wall ("no-wall limit"), and just at or below the ideal $n = 1$ limit with a perfectly conducting wall ("ideal-wall limit"). (The toroidal mode number of the magnetohydrodynamic (MHD) instability is designated by n.) Poor energy confinement may limit the obtainable β_N to values less than those set by stability limits and limit the duration of the high power phase of the discharge by more quickly exhausting the available input power. Confinement and β_N enter into the normalized fusion gain scale factor[9] $G = \beta_N H_{89} / q_{95}^2$, where H_{89} is the ratio of energy confinement time to the ITER L-confinement mode (L-mode) scaling,[10] and q_{95} is the safety factor at 95% of the normalized poloidal flux. G must be 0.3 to extrapolate to the fusion gain $Q = 5$ in an ITER steady-state scenario.[11] Finally density control is essential because as density increases, ECCD and neutral beam current drive (NBCD) drive decrease faster than bootstrap current increases.[5] At higher density, the electron cuclotron (EC) waves launched into the plasma can be reflected. ECCD at mid-radius is necessary to avoid the occurrence of 2/1 tearing modes.[12]

The work described in this paper is an extension and integration of earlier shape optimization studies. High triangularity[13,14] has been shown to increase the stability of the pedestal, resulting in higher pedestal pressure, but stronger, less frequent edge localized modes (ELMs). Pedestal stability and confinement were also found[15,16] to be sensitive to ζ, and magnetic divertor balance has been observed[17] to affect density and stored energy.

Here we report on further modeling and analysis of experiments that identify the optimum trade-off ζ and divertor balance for global stability, confinement, and density control for fully noninductive scenario discharges. In Sec. II, experimental results are presented that show confinement generally better at the lowest ζ attempted in scans. This is explained by a combination of higher pedestal pressure and reduced core transport. In Sec. III, modeling results are given that predict higher ideal $n = 1$ kink β_N-limits at low to intermediate ζ. This trend appears in the maximum experimentally sustained values of β_N. Ideal $n = 1$ stability analysis with the measured pressure and current density profiles and discharge shapes is in qualitative agreement with the modeling. In Sec. IV, we show how adjusting the magnetic divertor balance near DN at optimal ζ allows density control while still maintaining good confinement and high stability. The resulting density reduction allows more ECCD for avoiding 2/1 tearing modes and increasing the noninductive current. Section V discusses and highlights the use of these shape optimizations to sustain nearly all the plasma current non-inductively for longer than previously reported, and Sec. VI summarizes the main conclusions.

II. SQUARENESS AND CONFINEMENT

Optimization of squareness is possible because, unlike elongation and triangularity, squareness adjustments may be made without significantly moving the divertor strike points. The definition of ζ used in this paper differs from those given in previous reports.[15,16] Here we limit attention to upper and lower outer ζ, and define it for each with respect to a reference ellipse with major radius at the X-point and minor radius at the low-field side midplane separatrix, as shown in Fig. 1. Accordingly, a perfect ellipse or circle has $\zeta = 0$, a diamond has $\zeta < 0$, and shapes approaching rectangular have $\zeta \rightarrow 1$. Double null advanced tokamak discharges on DIII-D typically have elongation $\kappa \approx$ 1.8–1.9 and triangularity $\delta \approx 0.6$–0.65. These values allow the strike points to be placed close to the mouth of each divertor for good pumping. The scans described here are at nearly fixed κ and δ with the outer ζ in the range $\zeta = -0.25$ (i.e. “low”) to 0.05 (“high”).

A dedicated scan at low β_N shows the global energy confinement time is greatest at the low end of the measured ζ range. A series of double-null discharges were prepared the same way until 2.3 s when ζ was varied to a new value. Injected neutral beam power was directed by the plasma control system to maintain a target $\beta_N = 2.4$ in all discharges. This level was chosen to minimize MHD activity for several seconds in order to more clearly evaluate the effect of ζ on confinement. A semi-rigid shift of the plasma was also programmed near the end of each discharge to acquire higher spatial resolution measurements of pedestal profiles. Figure 2 shows the energy confinement time τ_E averaged for a steady 1-second period as a function of ζ calculated from equilibrium reconstructions using the EFIT code.[18] Low amplitude $m/n = 5/3$ and/or 3/2 modes were present in each, but the resulting confinement degradation estimate using the Chang-Callen "belt" model[19] is a loss of 5%–6% for all cases. The line-averaged density for all cases is in the range of 47%–52% of the Greenwald density, which is well below the approximate value of 60% typically required for partial divertor detachment.[20] There is roughly a 30% decrease in τ_E as ζ is varied from the lowest to highest values in the scan. Higher ζ shapes have greater volume, so the observed decrease in energy confinement is counter to the expectation in the H_{89} and H_{98y2} confinement scaling laws[10, 21] that predict confinement will improve with volume through R, a, and κ. These parameters are not changed in the ζ scans, and ζ does not enter into these scaling laws.

The confinement trend with ζ persists at high β_N. At high β_N it is more difficult to avoid MHD that can obscure the effect of shape on global confinement. Nonetheless, a series of discharges that probed the β_N limit dependence on ζ have common 100 ms MHD-free periods at high-β_N during which confinement may be compared. Figure 3 shows the time-traces of β_N for these discharges and the average of τ_E during the first 100 ms of the flattop in β_N as a function of the discharge ζ. The best energy confinement time for the lowest ζ is ~70% greater than that for the highest ζ, with $H_{98(y,2)}$ varying from 1.35 to 1.85.

Power balance calculations show increased transport correlated with measurements of increased turbulence at higher ζ. Figure 4 shows the ion thermal diffusivity profiles calculated by the ONETWO transport code[22] with measured temperature and density profiles as inputs for two of the low-β_N discharges in the ζ scan shown in Fig. 2. The low ζ discharge ($\zeta \approx -0.25$) has lower thermal transport across most of the profile than the higher ζ discharge ($\zeta \approx -0.10$). This difference is consistent with measurements of low-$k_\perp$ (≤ 2.5 cm^{-1}) density fluctuations made by a beam emission spectroscopy (BES) diagnostic.[23] Figure 5(a) shows the normalized density fluctuation power spectra at $\rho = 0.68$. The measured turbulence is higher over a broad frequency range for the higher ζ case, and it peaks at somewhat lower frequency than the low ζ case. The frequency shift corresponds to a poloidal turbulence velocity that is estimated to be about 15% greater for low ζ. Figure 5(b) shows the normalized density fluctuation in the range of 80–400 kHz is about a factor of 2 higher with higher ζ at all radii where measurements are available. Figure 6 shows the injected neutral beam torque and the total angular momentum for the discharges in Fig. 2 as a function of ζ. Momentum confinement must also be reduced at higher ζ because the total angular momentum decreases with ζ even though more torque is applied.

The confinement improvement with decreasing ζ is correlated with a simultaneous growth in pedestal pressure across the range of the experiments. High-resolution profile measurements of the electron density and temperature, and impurity ion density, temperature, and rotation are averaged over the last 20% of the ELM cycle. The main ion temperature is assumed to be equal to the impurity ion temperature, and the main ion density is calculated from charge balance assuming carbon is the only impurity. Fast ion density and temperature are calculated with the Nubeam code.[24] Using these we determine the total pedestal pressure profile prior to an ELM. The resulting pedestal pressure profiles for the discharges with $\zeta = -0.25$ and $\zeta = -0.1$ in Fig. 2 are compared in Fig. 7 with their shapes in the inset. The lower ζ discharge has ~10% greater pedestal pressure than the higher ζ discharge. This is consistent with a greater pedestal pressure gradient limit for ELM peeling-ballooning stability, as shown in Fig. 8. Here the stability space for edge current density and normalized pedestal pressure gradient α is calculated using the ELITE code[25] with measured profiles as input. The operating points for these discharges are shown with 15% uncertainty based on estimates of possible measurement systematic errors.[26] Each discharge operates very close to the ELM stability limit, but the lower ζ case stability boundary extends to greater α and this allows access to greater pedestal pressure. While the pedestal pressures in these two discharges differ by ~10% due to their shapes, both are under β_N feedback control, so their volume averaged pressures differ by less than 2%, with the low ζ case the greater. Less input power is required to match the same β_N with a higher pedestal pressure, improving confinement. The low ζ discharge pressure profile is greater than the high ζ discharge pressure profile everywhere inside the pedestal, so it is the difference in the volumes that makes the volume averaged pressures nearly equal. The ~19% better confinement time of the low ζ discharge is likely due in part to the higher pedestal pressure allowing a reduced input power, and also to the reduced core turbulence and transport that results from the lower power.

III. SQUARENESS AND STABILITY

Ideal MHD predictive modeling[27,28] suggests that ζ is a valuable control tool for optimizing global stability limits. Figure 9 shows the results of stability analysis performed on modeled equilibria. These are DN shapes with fixed κ and δ that are typical of DIII-D discharges. Pressure peaking factors and q_{min} were chosen based on expected advanced scenario operating points. In all cases the pressure profile including an H-mode pedestal was scaled to find the β_N limit for ideal external kink $n = 1$ modes for a range of ζ achievable in DIII-D. For each shape, the β_N limit was calculated by self-consistently adjusting the pressure, bootstrap current and total current profiles at fixed toroidal field. While the methods, profile models and codes used were not identical in each study, the trend of increased $n = 1$ ideal-wall β_N-limit with lower ζ is a common result.

On DIII-D, the experimentally obtained maximum sustainable β_N follows the same general trend with ζ as that predicted by the ideal-wall $n = 1$ modeling. This is shown in Fig. 10, where each point represents a different DN discharge. All discharges are formed identically until a ζ change that is completed ~100 ms before a programmed increase in the target β_N. Total current, κ and δ are held fixed. Dynamic error field correction using the DIII-D I-coils was employed for all discharges.[29] The minimum in the safety factor profile (q_{min}) was about 1.5 with q on axis (q_0) slightly greater than or equal to this at the time of the β_N increase. At each ζ, the target β_N was adjusted in successive discharges until the maximum β_N was found that could be sustained for at least a few hundred ms without the occurrence of any large amplitude MHD mode. The maximum achievable β_N was found to occur at intermediate ζ, with ~30% greater β_N than discharges with the highest ζ attempted.

Figure 11 compares the calculated $n = 1$ ideal-wall β_N-limit of a discharge with $\zeta = -0.13$ (low) to a discharge with $\zeta = +0.03$ (high). These were calculated using equilibrium reconstructions constrained by internal measurements as input to the CORSICA[30] code's TEQ inverse equilibrium solver[31] and DCON stability[32] packages. The measured β_N is shown for the discharges on the same plot. The superior stability of the lower ζ discharge is consistent with an observed broader, less peaked pressure profile that is known to improve stability.[33] The profile broadening is achieved as a result of the higher pedestal pressure allowed by this ζ. Improvement in the $n = 1$ stability as a direct response to more favorable field line curvature at this ζ cannot be ruled out.

For each shape, the high-β_N phase is terminated by a $m/n = 2/1$ tearing mode when β_N is near the calculated $n = 1$ ideal-wall limit. Figure 11 shows the Fourier-analyzed $n = 1$ RMS amplitude from a magnetic probe array for the two discharges to indicate when this occurs. The resulting island structure severely decreases energy confinement and can lead to a locked mode and disruption. The appearance of a resistive mode when β_N approaches an ideal limit is consistent with theory[34] that predicts the tearing mode stability index Δ' goes to infinity at the ideal limit, and may become large and positive as the ideal limit is approached.

IV. MAGNETIC DIVERTOR BALANCE AND DENSITY CONTROL

Magnetic divertor balance has been optimized for density reduction to increase the current the neutral beam and electron cyclotron systems are capable of driving. In DIII-D this balance is described by the parameter dRsep, which is the radial separation at the low-field side mid-plane between the flux surfaces connected to the upper and lower divertor X-points. An upper single null plasma has dRsep>0, a lower single null plasma has dRsep<0, and a double null (DN) plasma has dRsep=0. A series of DN discharges were identically prepared until a programmed change in dRsep in the middle of each. The dependence of the resulting line-averaged electron density on dRsep is plotted in Fig. 12(a), and Fig. 12(b) shows a cross section of DIII-D with the divertor structure and DN plasma. In all cases the ion $\boldsymbol{B}\times\nabla\boldsymbol{B}$ drift is directed toward the lower divertor. Thus when dRsep>0 the ion $\boldsymbol{B}\times\nabla\boldsymbol{B}$ drift points away from the dominant X-point.

About a 30% reduction in the line-averaged density is possible using a slightly unbalanced DN, corresponding to dRsep=+0.5 to +1.0 cm. This density reduction depends strongly on whether the ion $\boldsymbol{B}\times\nabla\boldsymbol{B}$ drift points toward or away from the dominant X-point. The reduction is much stronger when the ion $\boldsymbol{B}\times\nabla\boldsymbol{B}$ drift points *away* from the dominant X-point. Other discharges have shown that when the ion $\boldsymbol{B}\times\nabla\boldsymbol{B}$ drift direction is reversed (i.e. it points up) lower single null plasmas have lower density than upper single null plasmas.[17] Changes in dRsep are accomplished with minimal change to the squareness, and we find that the ~30% reduction in density by adjusting from dRsep=0 to 0.5 cm comes at the cost of only a ~10% reduction in energy confinement time. The causes of this improved density control are still under investigation. Modeling of experiments[35,36] using the two-dimensional fluid code UEDGE[37] suggests the $\boldsymbol{E}\times\boldsymbol{B}$

drifts in the dominant divertor private flux region may be important for affecting the distribution of divertor D_α recycling and neutral density at the pump openings.

V. SHAPE OPTIMIZED FULLY NONINDUCTIVE SCENARIO

These studies identify a high triangularity, moderate squareness shape with a slight divertor bias away from the ion $\boldsymbol{B} \times \nabla \boldsymbol{B}$ drift direction as the optimal for fully noninductive scenario experiments. Upper and lower outer $\zeta = -0.13$ affords the greatest achievable β_N, with good confinement, and dRsep=0.5 to 1.0 cm with the ion $\boldsymbol{B} \times \nabla \boldsymbol{B}$ drift directed down maintains a sufficiently low density for auxiliary noninductive current drive.

Advanced scenario discharges are formed with early neutral beam heating to limit the current profile penetration and achieve elevated q_{min} and a broad pressure profile. The optimized shape is produced at the time of the L- to H-mode transition, usually near $t \sim$ 500 ms. The use of only co-I_{p} injected neutral beams maximizes NBCD and toroidal rotation. Error field correction is employed using the DIII-D I-coil set to avoid the occurrence of locked modes as the pressure is increased. At about $t \sim$ 2.5 s the neutral beam power is ramped up and programmed to maintain $\beta_N = 3.8$ for as long as the required NB power is available, or until a $n = 1$ mode is detected. Approximately 3 MW of ECCD are applied at this time from five 110 GHz gyrotrons. The ECCD is distributed with a relatively broad profile between $\rho = 0.35$ and 0.55 and is found to allow reproducible operation without the occurrence of deleterious 2/1 tearing modes.

Figure 13 shows the results of one such discharge with $B_{\mathrm{T}} =$ 1.75 T and $I_{\mathrm{p}} =$ 0.9 MA. β_N is sustained between 3.5 and 3.9 for almost 2 seconds until the available neutral beam energy is exhausted. q_{min} is about 1.6 and H_{98y2} is about 1.5 at the beginning of this phase. The surface loop voltage is negative or within 10 mV of zero for about 1.7 s, which is about 70% of τ_R ($\tau_R \approx 2.5$ s in these discharges). This is a good indication that the inductive current is small during this time. A ONETWO transport code simulation of the current profile evolution was performed using the measured kinetic profiles as input. Bootstrap current is calculated using the Sauter model,[38] neutral beam current is calculated using the NUBEAM[24] model with a uniform, ad hoc anomalous fast ion diffusion of 1.0 m^2/s (required to match the stored energy), and ECCD is calculated using the TORAY-GA code.[39] The simulation predicts f_{NI} near 1 and f_{BS} near 0.65 during the high β_N phase. These results improve upon previously reported[5] work that obtained maximum sustained β_N near 3.2 to 3.6 with ~0 surface loop voltage for 40% of τ_R.

In these discharges, β_N is ~30% above the calculated no-wall $n = 1$ stability limit, and approximately at the ideal-wall $n = 1$ limit. The calculated ideal $n = \infty$ ballooning limit is just above the achieved β_N, at about $\beta_N \sim 4$. Stability to 2/1 tearing modes is maintained as long as the wide deposition ECCD is applied. The high β_N phase is limited by the neutral beam pulse length. Relatively low amplitude 5/3 tearing modes are typically observed that future q-profile optimization (i.e. higher q_{min}) may help to avoid.

Measurement and simulation show the inductive current density is small everywhere during the high β_N phase. Figure 14(a) shows the flux surface averaged total and inductive $J_{||}$ profiles from EFIT reconstructions constrained by motional Stark effect[40] and pressure profile measurements. The inductive component is calculated using a loop voltage analysis[41] that uses neoclassical conductivity and time derivatives of poloidal flux from a series of EFITs to obtain $\sigma E_{||}$. The resulting inductive current density is close to zero everywhere. Figure 14(b) shows the current component profiles at the same time calculated by the time-dependent ONETWO simulation. The simulated inductive current is in rough agreement with that determined from the V_{loop} analysis. There are uncertainties in the bootstrap and neutral beam current models near the axis that are transferred to the inductive current. For example, lower fast ion diffusion and/or higher core bootstrap current would further reduce the inductive current on axis.

VI. SUMMARY

Shape-optimized DIII-D discharges have simultaneously achieved higher β_N, higher bootstrap fraction, and longer duration of $f_{NI} \sim 1$ than previously reported work.[5] A baseline double-null, high triangularity shape has been shown to still have significant performance dependence on squareness, which is a convenient parameter that may be adjusted without affecting divertor coupling. Squareness optimization allows a ~30% variation in the achievable β_N resulting from an ideal-wall $n = 1$ stability dependence on this parameter. The energy confinement time varies about 30% with squareness at low fixed β_N, and about 70% when β_N is taken to its limit in each case. This results from pedestal pressure and core transport dependence on squareness. Experiment and modeling identify low to intermediate squareness as having greater pedestal and global stability than high squareness. A slight imbalance of the double null divertor with the main X-point opposite the ion $\boldsymbol{B} \times \nabla \boldsymbol{B}$ drift direction is used to reduce the line-averaged density ~30% compared to a balanced double-null, or the case with the ion $\boldsymbol{B} \times \nabla \boldsymbol{B}$ drift toward the X-point. This is understood to result from more favorable $\boldsymbol{E} \times \boldsymbol{B}$ drifts in the divertor private flux region in the first case. The ideal $n = 1$ stability, pedestal stability, and particle control dependence are all described by theoretical models that can be used to optimize future tokamak designs.

Acknowledgment

This work was performed in part under the auspices of the U.S. Department of Energy by Lawrence Livermore National Laboratory under DE-AC52-07NA27344, General Atomics under DE-FC02-04ER54698, University of California-Los Angeles under DE-FG03-01ER54615, Princeton Plasma Physics Laboratory under DE-AC02-76CH03073, Oak Ridge National Laboratory under DE-AC05-00OR22725, Columbia University under DE-FG02-89ER53297, and University of Wisconsin-Madison under DE-FG02-89ER53296.

References

[1] J.L Luxon, Nucl. Fusion, **42**, 614 (2002).

[2] P.A. Politzer, A.W. Hyatt, T.C. Luce, *et al.*, Nucl. Fusion **45**, 417 (2005).

[3] R.J. Bickerton, J.W. Connor and J.B. Taylor, Nature Phys. Sci. **229**, 110 (1971).

[4] C.M. Greenfield, M. Murakami, J.R. Ferron, *et al.*, Phys. Plasmas **11**, 2616 (2004).

[5] M. Murakami, M.R. Wade, C.M. Greenfield, *et al.*, Phys. Plasmas **13**, 056106 (2006).

[6] M. Murakami, C.M. Greenfield, M.R. Wade. *et al.*, Nucl. Fusion **45**, 1419 (2005).

[7] D.R. Mikkelsen, Phys. Fluids B **1**, 333 (1989).

[8] M.R. Wade, M. Murakami, T.C. Luce, *et al.*, Nucl. Fusion **43**, 634 (2003).

[9] T.C. Luce, Fusion Sci. Technol. **48**, 294004 (2005).

[10] P.N. Yushmanov, T. Takizuka, K.S. Riedel, *et al.*, Nucl. Fusion **30**, 1999 (1990).

[11] A.R. Polevoi *et al.*, Nucl. Fusion **45**, 1451 (2005).

[12] J.R. Ferron, V. Basiuk, T.A. Casper, C.D. Challis, J.C. DeBoo, E.J. Doyle, Q. Gao, A.M. Garofalo, C.M. Greenfield, C.T. Holcomb, *et al.,* Fusion Energy 2008 (Proc. 22nd Int. Conf., Geneva, 2008) (Vienna: IAEA) Paper EX/P4-27, http://www-pub.iaea.org/MTCD/Meetings/fec2008pp.asp and to be submitted for publication in Nucl. Fusion.

[13] T.H. Osborne, J.R. Ferron, R.J. Groebner, *et al.*, Plasma Phys. Control. Fusion **42**, A175 (2000).

[14] A.E. Hubbard, Plasma Phys. Control. Fusion **42**, A15 (2000).

[15] J.R. Ferron, M.S. Chu, G.L. Jackson, *et al.*, Phys. Plasmas **7**, 1976 (2000).

[16] A.W. Leonard, T.A. Casper, R.J. Groebner, *et al.*, Nucl. Fusion **47**, 552 (2007).

[17] T.W. Petrie, J.G. Watkins, L.R. Baylor, *et al.*, J. Nucl. Mater. **313-316**, 834 (2003).

[18] L.L. Lao, J.R. Ferron, R.J. Groebner, *et al.*, Nucl. Fusion **30**, 1035 (1990).

[19] Z. Chang, J.D. Callen, Nucl. Fusion **34**, 1309 (1994).

[20] T.W. Petrie, D.N. Hill, S.L. Allen, *et al.*, Nucl. Fusion **37**, 321 (1997).

[21] ITER Physics Basis, Nucl. Fusion **39**, 2175 (1999).

[22] H.E. St John, T.S. Taylor, Y.R. Lin-Liu, A.D. Turnbull, *Proceedings of the 15th International Conference on Plasma Physics and Controlled Nuclear Research 1994*, Seville, Spain, Vol. 3 (IAEA, Vienna, 1995) p. 603.

[23] G.R. McKee, R. Ashley, R. Durst, *et al.*, Rev. Sci. Instrum. **70**, 913 (1999).

[24] A. Pankin, D. McCune, R. Andre, *et al.,* Computer Physics Communications **159**, 157–184 (2004).

[25] P.B. Snyder, *et al.*, Phys. Plasmas **9**, 2037 (2002).

[26] A.W. Leonard, R.J. Groebner, T.H. Osborne, P.B. Snyder, Phys. Plasmas **15**, 056114 (2008).

[27] M.A. Makowski, T.A. Casper, J.R. Ferron, T.S. Taylor, A.D. Turnbull, “Effect of Profiles and Shape on Ideal Stability of Advanced Tokamak Equilibria,” *Proceedings of the 30th European Conference on Controlled Fusion and Plasma Physics, St. Petersburg, 2003,* edited by R. Koch and S. Lebev (European Physical Society, Geneva, 2003), ECA Vol. 27A, P-2.113, http://epsppd.epfl.ch/StPetersburg/PDF/P2_113.PDF

[28] C.E. Kessel, J.R. Ferron, C.M. Greenfield, J.E. Menard, and T.S. Taylor, “Shape Optimization for DIII-D Advanced Tokamak Plasmas,” *Proceedings of the 30th European Conference on Controlled Fusion and Plasma Physics, St. Petersburg,*

2003, edited by R. Koch and S. Lebedev (European Physical Society, Geneva, 2003), ECA Vol. 27A, P-4.044, http://epsppd.epfl.ch/StPetersburg/PDF/P4_044.PDF

[29] A.M. Garofalo, R.J. La Haye, J.T. Scoville, Nucl. Fusion **42**, 1335 (2002).

[30] J.A. Crotinger, L. LoDestro, L.D. Pearlstein, A. Tarditi, T.A. Casper, E.B. Hooper, "CORSICA: A Comprehensive Simulation of Toroidal Magnetic Fusion Devices," Final Report to the LDRD Program, LLNL Technical Report UCRL-ID-126284, 21 March 1997.

[31] L.L. Lodestro, L.D. Pearlstein, Phys. Plasmas **1**, 90 (1994).

[32] A.H. Glasser, M.S. Chance, Bull. Am. Phys. Soc. **42**, 1848 (1997).

[33] J.R. Ferron, T.A. Casper, E.J. Doyle, A.M. Garofalo, *et al.*, Phys. Plasmas **12**, 056126 (2005).

[34] D.P. Brennan, R.J. La Haye, A.D. Turnbull, M.S. Chu, *et al.*, Phys. Plasmas **10**, 1643, (2003).

[35] M. Groth, *et al.,* J. Nucl. Mater. **337–339**, 425 (2005).

[36] T.W. Petrie, N.H. Brooks, M.E. Fenstermacher, M. Groth, A.W. Hyatt, C.J. Lasnier, A.W. Leonard, G.D. Porter, M.J. Schaffer, M.R. Wade, J.G. Watkins, and W.P. West, "Sensitivity of Injected Argon Behavior to Changes in Magnetic Balance in Double-null Plasmas in DIII-D," accepted for publication in J. Nucl. Mater.

[37] T.D. Rognlien, *et al.*, Plasma Phys. **34**, 362 (1994).

[38] O. Sauter, C. Angioni, Y.R. Lin-Liu, Phys. Plasmas **6**, 2834 (1999).

[39] Y.R. Lin-Liu, V.S. Chan, R. Prater, Phys. Plasmas **10**, 4064 (2003).

[40] B.W. Rice, K.H. Burrell, L.L. Lao, Y.R. Lin-Liu, Phys. Rev. Lett. **79**, 2694 (1997).

[41] C.B. Forest, K. Kupfer, T.C. Luce, *et al.*, Phys. Rev. Lett. **73**, 2444 (1994).

[42] L.C. Bernard, F.J. Helton, R.W. Moore, Comput. Phys. Commun. **24**, 377 (1981).

[43] R.C. Grimm, R.L. Dewar, J. Manickam, J. Comput. Phys. **49**, 94 (1983).

Figure Captions

Fig 1. Definition of shape parameter squareness ζ, showing extreme cases. The shape shown is a model double-null shape, and the dashed curve is a reference ellipse used to calculate the squareness of the upper right quadrant. The major radius of the ellipse is at the upper X-point, and the minor radius of the ellipse is at the separatrix at the low-field side midplane.

Fig 2. (a) Double null discharge squareness variation used in scans and (b) the resulting global energy confinement time as a function of squareness.

Fig 3. (a) Global energy confinement time as a function of squareness at high β_N and (b) $\beta_N(t)$ for these discharges. The vertical band denotes the MHD-free period for all discharges during which τ_E in (a) is taken.

Fig 4. Ion thermal diffusivities calculated by the ONETWO transport code versus normalized radius ρ for the $\zeta = -0.25$ (low) and $\zeta = -0.10$ (higher) discharges shown in Fig. 2. The normalized radius ρ is defined as the square root of the toroidal flux normalized to the edge value.

Fig. 5. BES measurements of density fluctuation level for high and low squareness discharges shown in Fig. 4. (a) Density fluctuation power spectra for the different shapes are shown at $\rho = 0.68$. (b) Profiles of normalized density fluctuation integrated over f = 80–400 kHz as a function of normalized radius.

Fig. 6. Total injected torque and angular momentum as a function of squareness for the discharges shown in Fig. 2.

Fig. 7. Comparison of H-mode pedestal pressures for the low and higher squareness discharges analyzed in Fig. 4

Fig. 8. ELITE stability code calculation of the ELM peeling-ballooning stability boundaries for the discharges shown in Fig. 7, and their operating points. The high squareness case is in red and low squareness case is in blue.

Fig. 9. Predictive modeling of the ideal $n = 1$ external kink stability as a function of squareness. (a) DCON and GATO[42] modeling of a set of equilibria with $\kappa = 1.9$, $\delta = 0.65$, $P_0 / \langle P \rangle = 2.5$, $q_{\min} > 2$. (b) PEST2[43] modeling of ideal-wall and no-wall limits for a different set of equilibria with $\kappa = 1.8$, $\delta = 0.65$, $P_0 / \langle P \rangle =$ 2.72–2.85, $q_{\min} > 2$. $P_0 / \langle P \rangle$ is the pressure peaking factor, where P_0 is the pressure on axis, and $\langle P \rangle$ is the volume-averaged pressure.

Fig. 10. Maximum sustained β_N as a function of squareness.

Fig. 11. Calculated ideal-wall $n = 1$ β_N-limit using DCON stability code (dashed), measured β_N, and measured $n = 1$ rms amplitude from magnetic probes for two discharges in the ζ-scan shown in Fig. 11. The blue curves are for a discharge with $\zeta = -0.13$ and the red curves are for a discharge with $\zeta = +0.03$.

Fig. 12. Line-averaged electron density as a function of magnetic divertor balance parameter dRsep. In these discharges the ion $B \times \nabla B$ drift direction is always toward the

bottom divertor.

Fig. 13. Shape optimized discharges with long pulse ECCD achieve high β_N, nearly fully noninductive conditions. (a) β_N and ECCD, (b) Measured surface loop voltage, (c) Calculated noninductive and bootstrap current fractions.

Fig. 14. Measurements and simulations of the current density components of the discharge shown in Fig. 13. (a) Kinetic EFIT flux surface-averaged total- and inductive-parallel current density profiles at $t = 3.750$ s. A loop voltage analysis with a 550 ms averaging window is used to compute the inductive component. (b) Current components calculated by a ONETWO transport code current simulation at $t = 3.740$ s. An anomalous, uniform fast ion diffusion of 1.0 $\mathrm{m^2/s}$ was used.

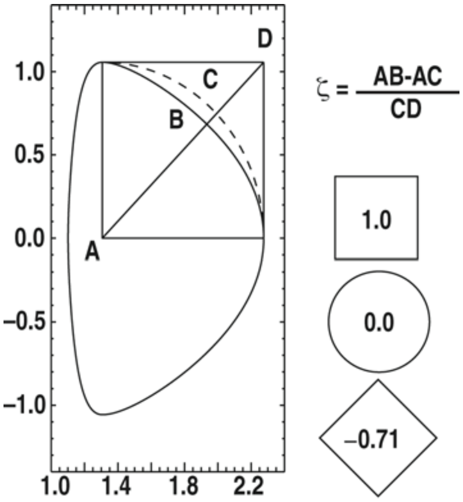
D
C
B
A
$\zeta = \frac{AB-AC}{CD}$
1.0
0.0
−0.71
1.0
0.5
0.0
−0.5
−1.0
1.0
1.4
1.8
2.2

Fig. 1

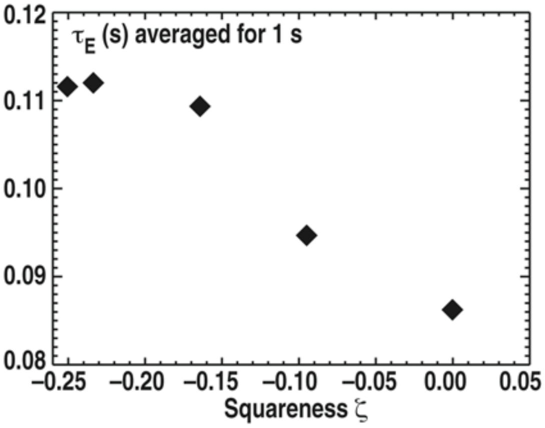

Fig. 2

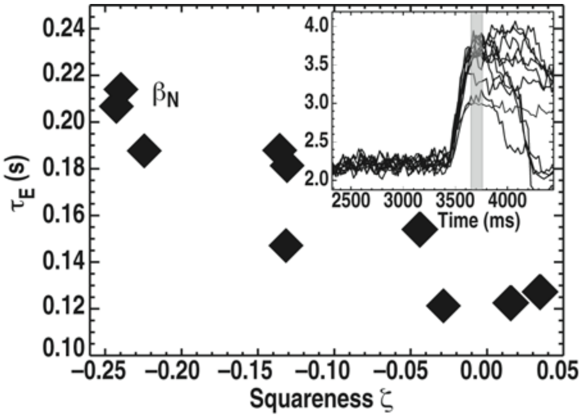

Fig. 3

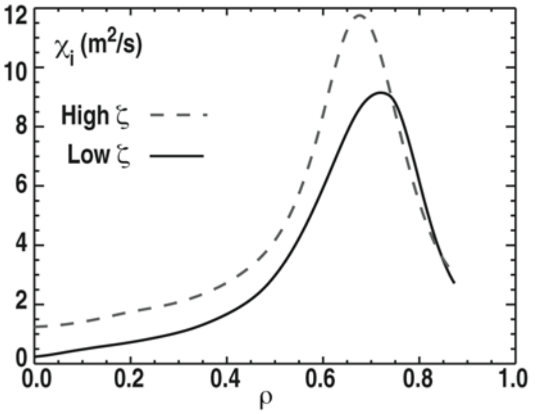
χ_i (m^2/s)
High ζ
Low ζ
12
10
8
6
4
2
0
0.0
0.2
0.4
0.6
0.8
1.0
ρ

Fig. 4

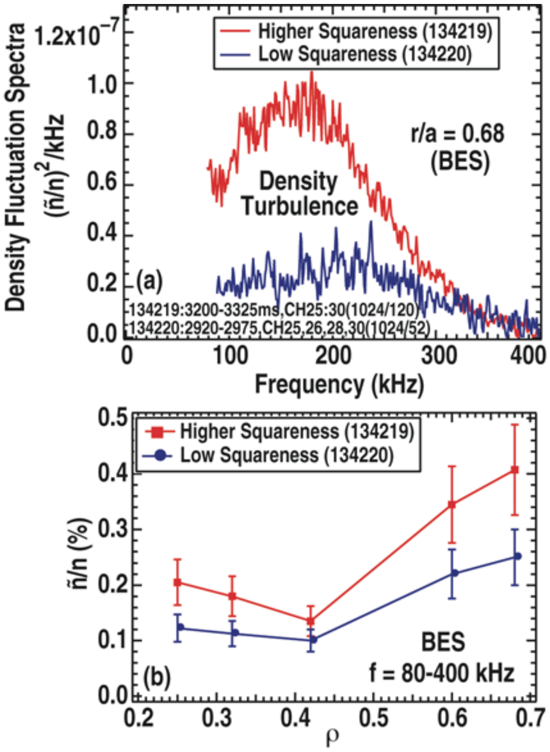
Density Fluctuation Spectra
$(\tilde{n}/n)^2$/kHz
1.2x10^{-7}
1.0
0.8
0.6
0.4
0.2
0.0
Higher Squareness (134219)
Low Squareness (134220)
r/a = 0.68
(BES)
Density
Turbulence
(a)
134219:3200-3325ms,CH25:30(1024/120)
134220:2920-2975,CH25,26,28,30(1024/52)
0
100
200
300
400
Frequency (kHz)
0.5
0.4
0.3
0.2
0.1
0.0
$\tilde{n}/n$ (%)
Higher Squareness (134219)
Low Squareness (134220)
BES
f = 80-400 kHz
(b)
0.2
0.3
0.4
0.5
0.6
0.7
ρ

Fig. 5

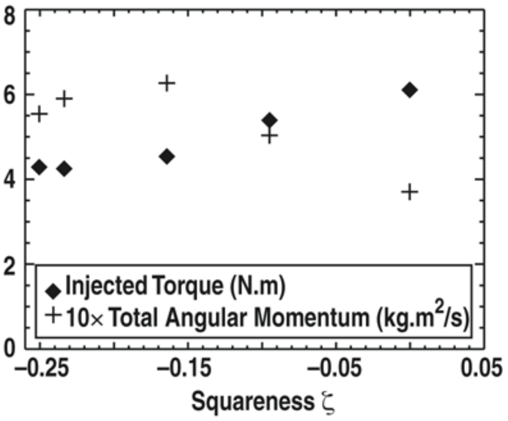

Fig. 6

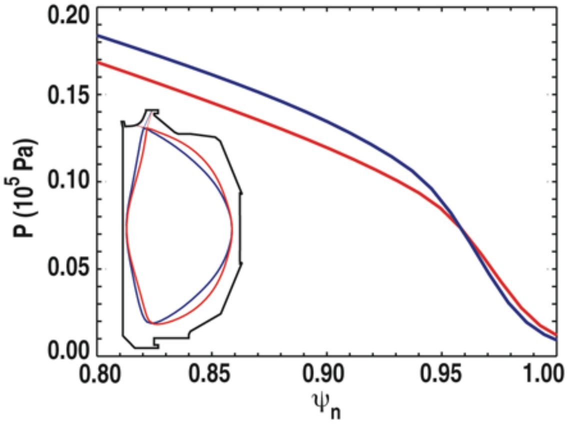

Fig. 7

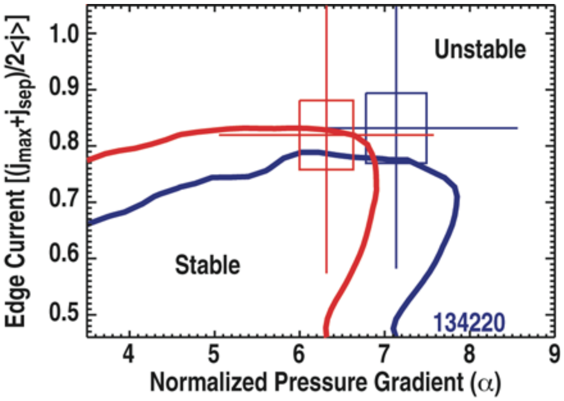

Fig. 8

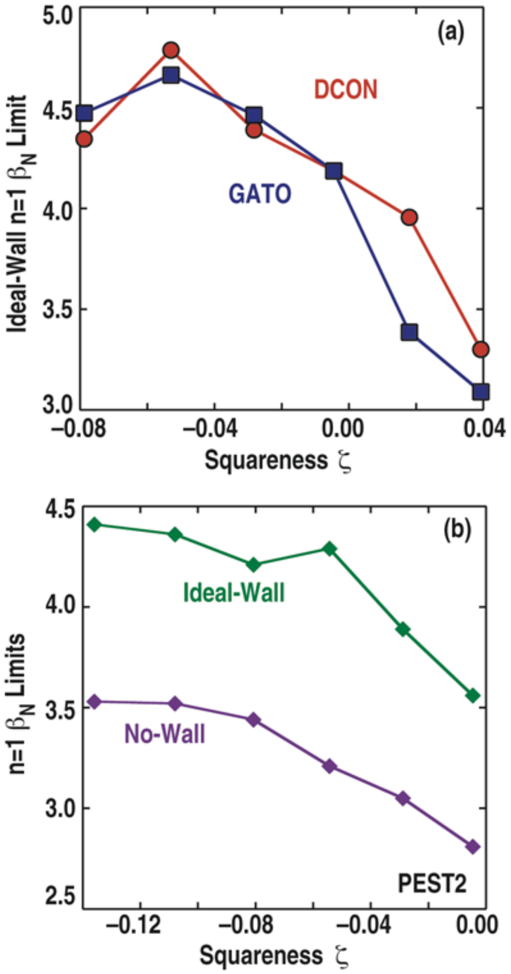
(a)
Ideal-Wall n=1 β_N Limit
5.0
4.5
4.0
3.5
3.0
DCON
GATO
–0.08
–0.04
0.00
0.04
Squareness ζ
(b)
n=1 β_N Limits
4.5
4.0
3.5
3.0
2.5
Ideal-Wall
No-Wall
PEST2
–0.12
–0.08
–0.04
0.00
Squareness ζ

Fig. 9

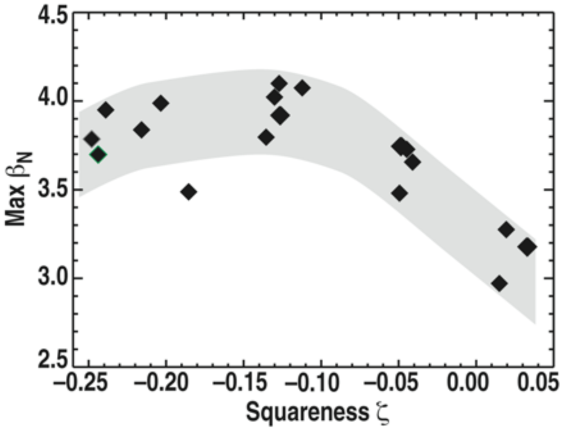
Max β_N
4.5
4.0
3.5
3.0
2.5
–0.25
–0.20
–0.15
–0.10
–0.05
0.00
0.05
Squareness ζ

Fig. 10

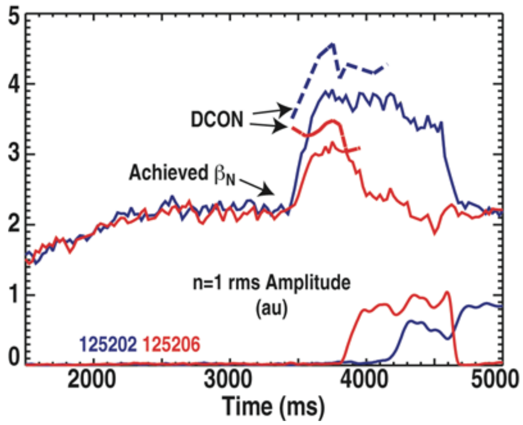

Fig. 11

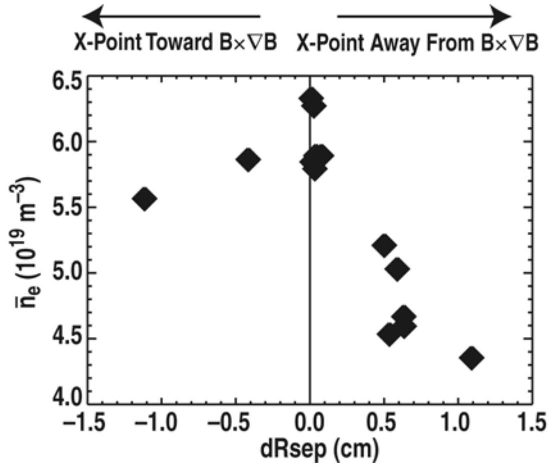

Fig. 12

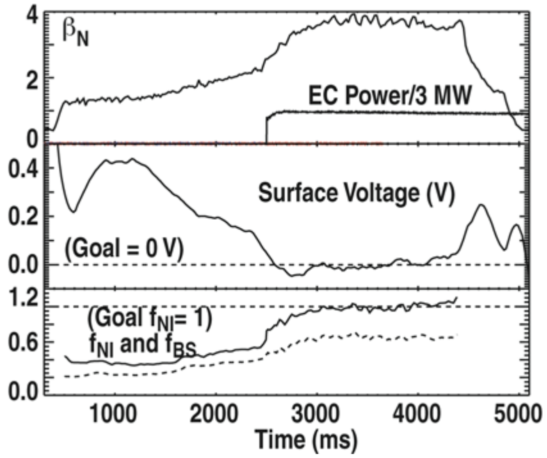

Fig. 13

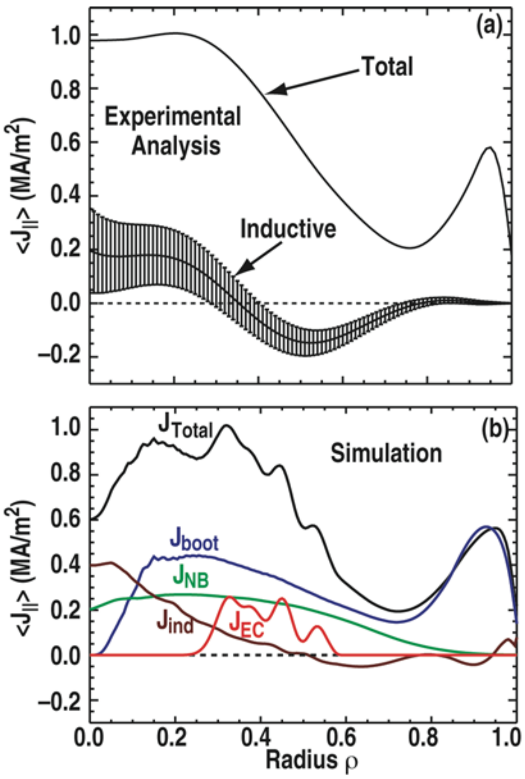
(a)
Total
Experimental Analysis
Inductive
$\langle J_{\|} \rangle$ (MA/m^2)
1.0
0.8
0.6
0.4
0.2
0.0
−0.2
(b)
J_{Total}
Simulation
J_{boot}
J_{NB}
J_{ind}
J_{EC}
$\langle J_{\|} \rangle$ (MA/m^2)
1.0
0.8
0.6
0.4
0.2
0.0
−0.2
0.0
0.2
0.4
0.6
0.8
1.0
Radius ρ

Fig. 14